

# Photoluminescence analysis of intragrain defects in multicrystalline silicon wafers for solar cells

H. Sugimoto,<sup>a)</sup> K. Araki, and M. Tajima

*Institute of Space and Astronautical Science, Japan Aerospace Exploration Agency, 3-1-1 Yoshinodai, Sagami-hara, Kanagawa 229-8510, Japan*

T. Eguchi

*Dai-ichi Dentsu Co., 1-54-1 Shimoishihara, Chofu, Tokyo 182-0034, Japan*

I. Yamaga

*Dai-ichi Kiden Co., 1-54-1 Shimoishihara, Chofu, Tokyo 182-0034, Japan*

M. Dhamrin, K. Kamisako, and T. Saitoh

*Tokyo University of Agriculture & Technology, 2-24-16, Naka-cho, Koganei, Tokyo 184-8588, Japan*

(Received 29 May 2007; accepted 12 July 2007; published online 7 September 2007)

Structures of intragrain defects were investigated by photoluminescence (PL) mapping tomography in multicrystalline silicon wafers for solar cells. PL dark patterns were observed in short minority carrier diffusion length regions, and we confirmed that the patterns came from the intragrain defects. The tomography revealed that the defects have planelike structures extended to the crystal growth direction. We also found that the growth conditions affect the structures of the defects: slower solidification leads to larger defects with lower density. Origins of the defects were analyzed by low-temperature PL spectroscopy, electron backscatter diffraction pattern measurement and etch-pit observation. We concluded that the defects are metal contaminated dislocation clusters which originate from small-angle grain boundaries. © 2007 American Institute of Physics.

[DOI: [10.1063/1.2776003](https://doi.org/10.1063/1.2776003)]

## I. INTRODUCTION

Photovoltaic energy is attracting much attention as a clean and sustainable energy, and the production of solar cells is expanding extensively. Multicrystalline Si (mc-Si) solar cells have become the dominant product due to their advantages of high-efficiency and low-cost. In mc-Si cells, there are numerous defects, such as grain boundaries (GBs) and dislocations, which act as a carrier recombination center and degrade the conversion efficiency. Restraining the mischief of GBs has been largely achieved by enlarging the grain size and restricting the appearance of active GBs, and now high quality wafers which have a minority carrier diffusion length of more than 400  $\mu\text{m}$  have been obtained.<sup>1</sup> Not only the optimization of crystal growth condition, but also gettering and passivation processes have contributed to improving the efficiency.<sup>2,3</sup> However, the present wafer quality of mc-Si cells is still less sufficient than single crystalline Si cells. The photovoltaic industry is now requiring further high quality mc-Si wafers to fabricate much higher-efficiency cells. Under these circumstances, the cell performance has been greatly limited by intragrain defects.<sup>4</sup> The authors have reported on the electrical activities of the intragrain defects in mc-Si wafers, and shown that these defects degrade the wafer quality greatly.<sup>5,6</sup> Furthermore, understanding their structures and origins is essential to the development of high quality mc-Si wafers.

Photoluminescence (PL) mapping is useful to characterize the distributions of defects in semiconductors. To investigate the three-dimensional structures of the defects, we developed a PL mapping tomography technique. Low-temperature PL spectroscopy is also a powerful tool for analyzing the origins of the defects. In this article, we disclose the structures and the origins of the intragrain defects by using PL techniques in collaboration with electron backscatter diffraction pattern (EBSP) measurement and etch-pit observation.

II. EXPERIMENTAL TECHNIQUES

### A. Samples

The mc-Si wafers used in this study were boron doped *p* type with a resistivity ranging from 1.0 to 1.5  $\Omega\text{cm}$ , a size of  $180 \times 130\text{ mm}^2$  and a thickness of 2.8 mm. They were sliced parallel to the crystal growth direction from two types of ingots fabricated by a unidirectional solidification technique<sup>1</sup> with rapid and slow solidifications. Any sawing damage was etched off by  $\text{HNO}_3/\text{HF}$  solution, and then the samples were rinsed in pure water following 5% HF etching. Before the PL measurement, distributions of minority carrier diffusion length were measured by surface photovoltage technique.

### B. Experimental conditions

We performed PL mapping tomography to investigate the three-dimensional structure of the intragrain defects. This technique was a repetition of PL mapping and thinning the samples with the  $\text{HNO}_3/\text{HF}$  etching. The repetition was performed four times, and both sides of the samples were char-

<sup>a)</sup>Electronic mail: [sugimoto@isas.jaxa.jp](mailto:sugimoto@isas.jaxa.jp)

acterized by the PL mapping followed by an etching of about  $100\text{ }\mu\text{m}$ /side each time. For the tomography, we used blocks of  $30\times 30\text{ mm}^2$  cut from the short diffusion length regions of the rapidly and slowly solidified wafers. Not only the vertical surfaces of samples parallel to the growth direction, but also the horizontal surfaces perpendicular to it with an area of  $30\times 2.8\text{ mm}^2$  were characterized by the PL mapping.

Macroscopic and microscopic PL mappings were performed at room temperature using 532 nm line of a Nd:YVO<sub>4</sub> laser as an excitation source. The excitation power of the macroscopic and microscopic mapping was about 10 and 0.1 mW, and the laser diameter was set about 300 and  $10\text{ }\mu\text{m}$ , respectively. The mapping system had an accurate and fast X-Y stage with position-repeatability as high as  $0.3\text{ }\mu\text{m}$  and a maximum translation speed of  $100\text{ mm/s}$ .<sup>7</sup> Luminescence light was collected by the objective, passed through the band-pass filters with a transmission band of 1050–1230 nm to extract the spectral component of the band edge emission, and detected by a cooled InGaAs photomultiplier (Hamamatsu R5509-72).

Origins of the intragrain defects were analyzed by low-temperature PL spectroscopy, electron backscatter diffraction pattern (EBSP) measurement and etch-pit observation. The low-temperature PL spectroscopy was performed at liquid-He temperature (4.2 K) under the excitation of the same laser as the PL mapping. The excitation power and laser beam diameter was 5 mW and 1 mm, respectively. PL from samples was analyzed with a monochromator (Jobin Yvon HR320,  $f=320\text{ mm}$ ,  $F=4.2$ ) with a 600 groove/mm grating blazed at  $1.0\text{ }\mu\text{m}$  and was detected by a Ge pin diode (Northcoast EO-817L) cooled at 77 K. The detected signal was processed with a lock-in technique. The spectral response of the measurement system was calibrated with blackbody radiation.

We performed the EBSP measurement to understand crystallographic orientations and types of GBs. The EBSP image was obtained from the intragrain defect regions of the horizontal surfaces. An area of  $2\times 2\text{ mm}^2$  was scanned with the pitch of  $10\text{ }\mu\text{m}$ , and the maximum resolution of misorientation was about  $2^\circ$ . To assess the distribution of dislocations, the etch pits of the same area were observed as of the EBSP measurement. Samples were etched with Dash-etching solution<sup>8,9</sup> for 90 min, and then we observed the etch pits with an optical microscope fitted with Nomarski differential interference optics.

### III. RESULTS AND DISCUSSIONS

#### A. Electrical activity of intragrain defects

Comparison between the macroscopic PL and the diffusion length mappings are shown in Fig. 1; upper and lower figures are the PL and diffusion length mappings, respectively. These samples were the latest mc-Si wafers and had a considerably long diffusion length of more than  $500\text{ }\mu\text{m}$ , however, there were also regions with quite a short diffusion length. Due to the highly spatial resolution of PL mapping, we are able to recognize dark-line patterns in these short diffusion length regions. Grains can be distinguished by the

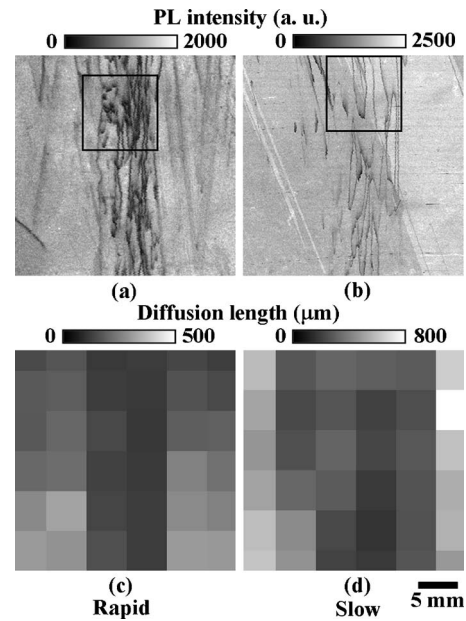


FIG. 1. Comparison between (a) macroscopic PL and (c) minority carrier diffusion length mapping on intragrain defect region of rapidly solidified wafer. That of slowly solidified one is also shown in (b) and (d). These mappings were obtained from wafers sliced parallel to growth direction. Whiter region indicates higher PL intensity and longer diffusion length region. Spatial resolution of PL and diffusion length mappings was  $100\text{ }\mu\text{m}$  and 5 mm, respectively.

contrast of background in the PL mappings, and we learned that the dark-line patterns existed in the intragrain areas. This means that these patterns were ascribable to the intragrain defects. We found that these defects became the intensively active recombination center and greatly degraded the diffusion length, while the GBs were electrically less active. Strong correlation between the PL mapping and the diffusion length (or lifetime) mapping has been well established, and several authors have also reported that the defect region has high recombination activity.<sup>10,11</sup>

Effects of the growth condition on the formation of these defects were also of interest. In Fig. 1, the left and right figures were obtained from the rapidly and slowly solidified wafers, respectively. The latter had a larger defect, and had lower defect density than the rapidly solidified wafer, as shown in Figs. 1(a) and 1(b). This indicates that the size and density of the intragrain defects are controllable by the growth conditions.

#### B. Structures of intragrain defects

Photoluminescence mapping tomography was performed to determine the three-dimensional structures of the intragrain defects. Figure 2 shows part of the results of this mapping tomography on the intragrain defect regions. Upper and lower mappings were obtained from the rapidly and slowly solidified wafers, respectively. We zoomed in on the defect regions by the microscopic PL mapping, and these areas correspond to the square regions marked in Figs. 1(a) and 1(b), respectively. Left, center, and right figures are the microscopic PL mappings on front side of samples before the etching, and after the first and second etching, respectively. The PL mapping and thinning of the samples was repeated four

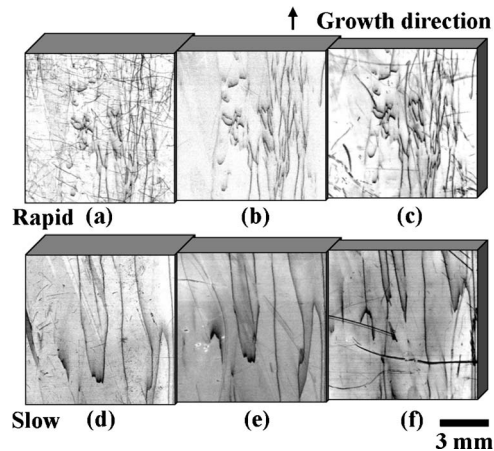


FIG. 2. PL mapping tomography on intragrain defect region of (a)–(c) rapidly and (d)–(f) slowly solidified wafer. Upper and lower mappings were obtained from identical area marked with square in Figs. 1(a) and 1(b), respectively. Left, center and right figures are microscopic PL mappings on front side of samples before etching, and after first and second etching, respectively. Wafers were thinned four times, and both sides of the samples were characterized by PL mapping followed by etching of about  $100\ \mu\text{m}$ /side each time. All mappings have spatial resolution of  $20\ \mu\text{m}$ .

times; both sides of the samples were characterized by the PL mapping followed each time by the etching of about  $100\ \mu\text{m}$ /side. As shown in Figs. 2(a) and 2(d), gradational dark patterns were observed on the samples before the etching, the gradational direction being along the growth direction. The patterns of the rapidly solidified wafer were smaller, and had higher defect density than those of the slowly solidified one. Positions of the patterns changed successively after the etching, as illustrated in Figs. 2(b), 2(c), 2(e), and 2(f), shifting to the growth direction each time. Backsides of the samples were also characterized, and the opposite behaviors of the patterns were observed; the gradational direction was opposite to the growth direction and the patterns also shifted to the opposite direction. We found that the direction of the shift corresponded to the gradational direction of the patterns on the same surfaces. From these facts, we believe that the defects had planelike structures as shown in Fig. 3. Figures 3(a) and 3(b) is the schematic illustration of the planelike defects observed on the front and back surfaces of samples, respectively. If the defects had the planelike structure, the patterns would shift successively. The depth of defect would also change successively, which created the gradational patterns; shallower defects caused greater degradation of the PL intensity because most of the

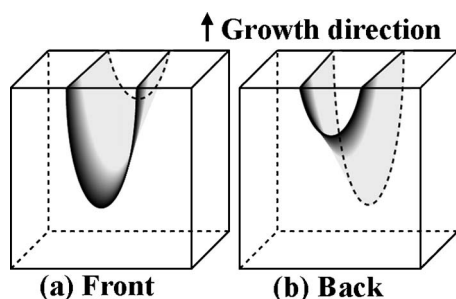


FIG. 3. Schematic illustrations of plane-like defects which were observed as gradational dark patterns in PL mapping on (a) front and (b) back surfaces.

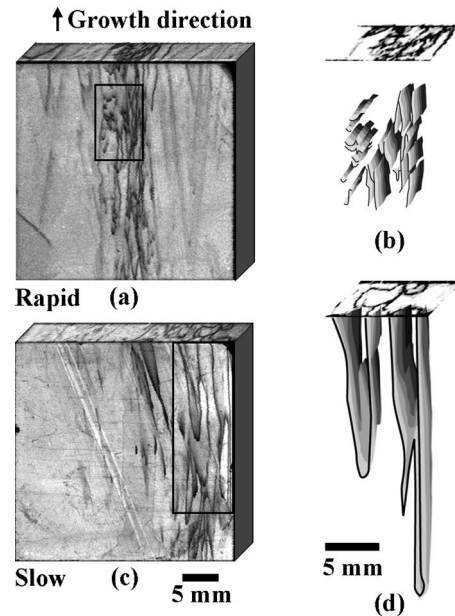


FIG. 4. Left figures are macroscopic PL mappings on vertical surface parallel to growth direction and horizontal surface perpendicular to it, and right figures are structures of intragrain defects determined from results of PL mapping tomography and PL mappings on vertical and horizontal surfaces. Upper and lower figures were obtained from rapidly and slowly solidified wafers, respectively. Spatial resolution of PL mapping was  $100\ \mu\text{m}$ .

excited carriers were produced nearby surface of the samples. For these reasons then, the shift directions corresponded to the gradational directions on the same surfaces. The determination of the probing depth of the PL mapping is important for analyzing the depth profiling of the defects. Though the penetration depth of the excitation laser is about  $1\ \mu\text{m}$ , the probing depth becomes much deeper because of the carrier diffusion. Figures 1(c) and 1(d) show that the defect regions had lower diffusion length than  $200\ \mu\text{m}$ , which means the PL probing depth was less than  $200\ \mu\text{m}$ . In areas closer to the defects, the probing depth may become shallower because of the lower diffusion length. Actually, we can estimate the probing depth around the defect regions experimentally; one gradational dark pattern had the gradational width of about  $600\ \mu\text{m}$ , and this defect had a lean of about  $5.2^\circ$  against the growth direction, which indicates that the probing depth was about  $55\ \mu\text{m}$ .

In addition to the PL mapping tomography, the PL mapping was also performed on the horizontal surface perpendicular to the growth direction. The macroscopic PL mappings on the vertical and horizontal surface of the rapidly and slowly solidified wafers are depicted in Figs. 4(a) and 4(c), respectively. Dark-line patterns were observed on the horizontal surfaces, however, there were no gradational patterns. The gradational patterns on the vertical surfaces corresponded well to the dark-line patterns on the horizontal surfaces. From the results of the PL mapping tomography and the PL mappings on the vertical and horizontal surfaces, we determined the structures of the intragrain defects which were observed as the dark-line patterns in the PL mapping. Defects of the rapidly solidified wafer had intermittent plane structures, and those of the slowly solidified one had cylindrical structures extending to the growth direction, as illus-



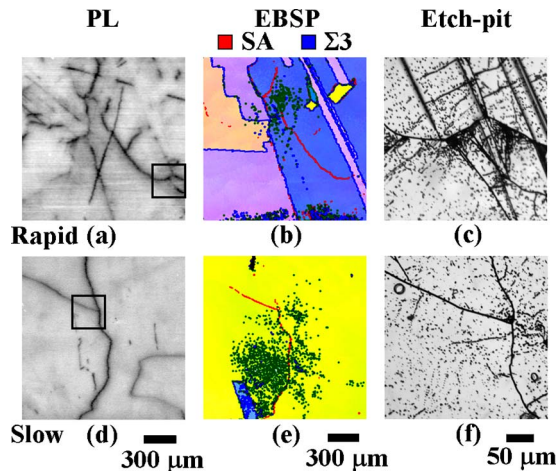


FIG. 5. (Color online) Comparison between (a) microscopic PL and (b) EBSP crystallographic orientation mapping on horizontal surface of rapidly solidified wafer. That of slowly solidified one is also shown in (d) and (e). For EBSP mapping, difference of color indicates different orientation. Red and blue lines show SA and  $\Sigma 3$  GBs, respectively. Dot patterns are due to roughness of sample surface. Spatial resolutions of PL and EBSP mapping were  $10\ \mu\text{m}$ , and maximum resolution of misorientation for present EBSP measurement was about  $2^\circ$ . Optical micrograph of etch-pits on identical area marked with square in (a) and (d) is also shown in (c) and (f), respectively. Note that blurry straight lines were not dislocation arrays but  $\Sigma 3$  GBs, and sharp lines were dislocation clusters.

trated in Figs. 4(b) and 4(d). We also confirmed that the growth conditions affected the size and density of the defects: slower solidification led to larger defects with lower density. These findings show that the defect structures can be controlled by regulating the growth conditions.

### C. Origins of intragrain defects

The origins of the intragrain defects were analyzed by the EBSP measurement and the etch-pit observation in addition to the microscopic PL mapping, as shown in Fig. 5. Comparison between the microscopic PL and the EBSP crystallographic orientation mapping on the horizontal surface of the rapidly solidified wafer is shown in Figs. 5(a) and 5(b), and that of the slowly solidified one in Figs. 5(d) and 5(e), respectively. Difference of background colors in the EBSP mapping indicates different orientation, and red and blue lines show small angle (SA) and  $\Sigma 3$  GBs, respectively. Dot patterns are due to the roughness of sample surfaces. We confirmed that the patterns of the  $\Sigma 3$  GBs did not correspond to the dark-line patterns in the PL mapping, but that the SA GBs corresponded well to them. Note that not all SA GBs were observed because of the shortage of angle resolution for the present EBSP measurement. In Figs. 5(b) and 5(e), we believe there were SA GBs with smaller misorientation than  $2^\circ$  at the PL dark-line pattern regions where the SA GBs were not detected by EBSP. Several researchers have also reported the strong recombination activity of the SA GBs by electron beam induced current (EBIC) measurement.<sup>12,13</sup> From these facts, we conclude that the intragrain defects were ascribable to the SA GBs.

Optical micrograph of the etch-pits on the identical area marked with a square in Figs. 5(a) and 5(d) is also shown in Figs. 5(c) and 5(f), respectively. Note that blurry straight

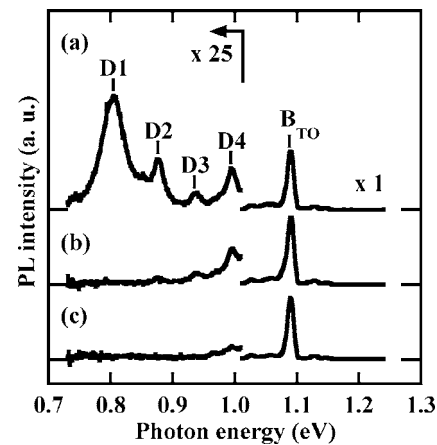


FIG. 6. PL spectra at 4.2 K from (a) intragrain defect region, (b)  $\Sigma 3$  GB region, and (c) long diffusion length region without defects or GBs.  $B_{\text{TO}}$  line is TO-phonon replica of boron bound exciton, and D1–D4 lines are dislocation-related lines. Symbol “ $\times 25$ ” denotes relative amplitude.

lines were not the dislocation arrays but the  $\Sigma 3$  GBs. At the dislocation clusters, the etch pits were piled up and looked like sharp lines. PL dark-line patterns corresponded to the sharp lines, which clearly shows that dislocation clusters existed at the PL dark-line patterns.

Low-temperature PL spectroscopy was also used to disclose the origins of the intragrain defects. Figure 6 shows the PL spectra at 4.2 K from the defect region where the dark-line patterns appeared, the region including the  $\Sigma 3$  GBs, and the long diffusion length region without the defect or GBs, respectively. The 1.093 eV line marked  $B_{\text{TO}}$  is the TO-phonon replica of the boron bound exciton. In the defect regions, dislocation-related lines labeled D1–D4 (Ref. 14) were observed besides the band edge emission. From the GB region, very weak D lines were observed, which indicates that there were a few dislocations. The D line signal from the long diffusion length region was below our detection limit. These results strongly support the idea that the defects are dislocation clusters. Ostapenko *et al.* have also demonstrated that the D lines are observed from the defect regions.<sup>15</sup> They also revealed that the 0.8 eV PL band corresponds to electrically active dislocation networks.<sup>10,15</sup> Concerning the 0.8 eV band, we will report in a forthcoming article. The generation of the D lines was reported to relate to the transition metal contamination.<sup>16,17</sup> By synchrotron radiation X-ray techniques, several authors have disclosed that the dislocation clusters are the preferred precipitation sites for metal impurities and these areas strongly correlate with low diffusion length regions.<sup>18,19</sup> The EBIC results have also shown that these contamination turns SA GBs into strong recombination centers.<sup>12,13</sup> These findings confirmed that the intragrain defects responsible for the PL dark patterns were the metal contaminated dislocation clusters which were ascribable to the SA GBs.

### IV. CONCLUSIONS

Comparison between PL and diffusion length mappings showed that the intragrain defects observed as the PL dark patterns greatly degraded the wafer quality. Structures of

these defects were investigated by PL mapping tomography, which revealed that the defects have planelike structures extending to the growth direction. We also found that the growth conditions affected the structures of the defects, slower solidification leading to larger defects with lower density. Origins of the defects were analyzed by low-temperature PL spectroscopy, EBSP measurement and etch-pit observation, and from the results we concluded that the defects are metal contaminated dislocation clusters which originated from SA GBs.

## ACKNOWLEDGMENTS

The authors would like to thank H. Ando, T. Yamazaki, and Dr. K. Nagashio for collaborative efforts in the EBSP measurement and the etch-pit observation, and Professor N. Usami, Professor Y. Ohshita, Professor A. Ogura, and Professor K. Kakimoto and Dr. K. Arafune, Dr. K. Kutsukake, and Dr. T. Minemoto for useful discussions and comments.

<sup>1</sup>T. Eguchi, T. Hirasawa, I. Yamaga, M. Dhamrin, T. Saitoh, and K. Kamisako, Proceedings of the 15th International Photovoltaic Sci. Eng. Conf., Shanghai, China, 116 (2005).

<sup>2</sup>W. Dimassi, M. Bouaicha, H. Nouri, S. Ben Nasrallah, and B. Bessais, Nucl. Instrum. Methods Phys. Res. B **253**, 264 (2006).

<sup>3</sup>R. Ludemann, Mater. Sci. Eng., B **58**, 86 (1999).

<sup>4</sup>Y. Ohshita, Y. Nishikawa, M. Tachibana, V. K. Tuong, T. Sasaki, N. Kojima, S. Tanaka, and M. Yamaguchi, J. Cryst. Growth **275**, e491 (2005).

<sup>5</sup>H. Sugimoto, M. Tajima, T. Eguchi, I. Yamaga, and T. Saitoh, Mater. Sci. Semicond. Process. **9**, 102 (2006).

<sup>6</sup>H. Sugimoto, M. Inoue, M. Tajima, A. Ogura, and Y. Ohshita, Jpn. J. Appl. Phys., Part 2 **45**, L641 (2006).

<sup>7</sup>M. Tajima, Z. Li, and R. Shimidzu, Jpn. J. Appl. Phys., Part 2 **41**, L1505 (2002).

<sup>8</sup>W. C. Dash, J. Appl. Phys. **27**, 1193 (1956).

<sup>9</sup>C. Okamoto, T. Minemoto, M. Murozono, H. Takakura, and Y. Hamakawa, Jpn. J. Appl. Phys., Part 1 **44**, 7805 (2005).

<sup>10</sup>I. Tarasov, S. Ostapenko, C. Haessler, and E.-U. Reisner, Mater. Sci. Eng., B **71**, 51 (2000).

<sup>11</sup>S. He, S. Danyluk, I. Tarasov, and S. Ostapenko, Appl. Phys. Lett. **89**, 111909 (2006).

<sup>12</sup>J. Chen, T. Sekiguchi, R. Xie, P. Ahmet, T. Chikyo, D. Yang, S. Ito, and F. Yin, Scr. Mater. **52**, 1211 (2005).

<sup>13</sup>W. Seifert, G. Morgenstern, and M. Kittler, Semicond. Sci. Technol. **8**, 1687 (1993).

<sup>14</sup>R. Sauer, J. Weber, and J. Stolz, Appl. Phys. A **36**, 1 (1985).

<sup>15</sup>S. Ostapenko, I. Tarasov, J. P. Kalejs, C. Haessler, and E.-U. Reisner, Semicond. Sci. Technol. **15**, 840 (2000).

<sup>16</sup>V. Higgs, E. C. Lightowers, and P. Kightley, Mater. Res. Soc. Symp. Proc. **163**, 57 (1990).

<sup>17</sup>M. Kittler, W. Seifert, T. Arguirov, I. Tarasov, and S. Ostapenko, Sol. Energy Mater. Sol. Cells **72**, 465 (2002).

<sup>18</sup>S. A. McHugo, Appl. Phys. Lett. **71**, 1984 (1997).

<sup>19</sup>T. Buonassisi, M. Heuer, O. F. Vyvenko, A. A. Istratov, E. R. Weber, Z. Cai, B. Lai, T. F. Cizek, and R. Schindler, Physica B (Amsterdam) **340–342**, 1137 (2003).